Structural Health Monitoring Special Issue

Institution of MECHANICAL ENGINEERS

Journal of MECHANICAL ENGINEERING SCIENCE

Proc IMechE Part C:
J Mechanical Engineering Science
0(0) 1–14

DOI: 10.1177/0954406216686996
journals.sagepub.com/home/pic

SAGE

Interaction of Lamb waves with rivet hole cracks from multiple directions

Md Yeasin Bhuiyan[1], Yanfeng Shen[2] and Victor Giurgiutiu[1]

Abstract

This paper presents the interaction of Lamb waves with rivet hole cracks from multiple directions of incident using the finite element approach. Lamb waves undergo scattering and mode conversion after interacting with the damage. Shear horizontal waves appear in the scattered waves because of the mode conversion. Instead of analyzing the whole large structure, the local damage area is analyzed using finite element analyses and analytical formulation is used to analyze the whole structure. The scatter fields are described in terms of wave damage interaction coefficients that involve scattering and mode conversion of Lamb waves. Lamb wave mode (S0 and A0) hit the damage from multiple directions and corresponding wave damage interaction coefficients are obtained around the damage. Harmonic analysis has been performed over the fundamental frequency domain and "scatter cubes" of complex-valued wave damage interaction coefficients are formed. The scatter cube provides the information of relative amplitude and phase of scattered waves around the damage that can be used for designing the sensor installation. An application based on real time domain signal has been illustrated for the problem of multiple-rivet-hole cracks using the scatter cubes with the analytical framework.

Keywords

Lamb wave, shear horizontal wave, structural health monitoring, nondestructive evaluation, scatter cube, sensor design

Date received: 19 May 2016; accepted: 6 December 2016

Introduction

The most important field of structural health monitoring (SHM) and nondestructive evaluation (NDE) deals with the detection of faults in structures, such as cracks, disbonds, delamination, impact damage, and corrosion thinning. Development of corrosion and fatigue cracks at the rivet holes and fasteners in the aircraft structures is the most frequent problem faced in the maintenance of aircraft. The cracks can grow to a critical size and threaten the structural integrity if they remain undetected. Ultrasonic guided wave techniques can be used for the detection of the emanating cracks from the rivet holes fastly, accurately, and efficiently as compared to the laborious point-by-point inspection technique.

State of the art

The problem of the detection of rivet hole cracks has been analyzed by the researchers of the NDE and SHM research field over the recent years. In 2009, the probability of detection (POD) by model-assisted approach has been demonstrated for the fatigue crack growth in wing lap joint, wing skin fastener holes, and airframe fastener holes.[1,2] In 2012, the use of the transfer function approach to the model-assisted POD is investigated by Bode et al.[3] through the inspection of a specimen of aircraft lap joint. However, the researchers emphasized the detection of fastener hole cracks mainly based on the nondestructive inspection (NDI) technique. In 2015, the SHM-based POD was obtained for the fatigue crack initiation in the lug with a wing attachment, which acted as a representative airplane component.[4] The piezoelectric wafer active sensor (PWAS) was used for transmitting and receiving signals with the center frequency domain of 200 to 1000 kHz. In order to detect the crack, six receiver sensors and nine excitation center frequencies were used to compute the damage index for a different combination of sensor and center frequency pair.

[1]Department of Mechanical Engineering, University of South Carolina, Columbia, SC, USA
[2]Department of Aerospace Engineering, University of Michigan, Ann Arbor, MI, USA

Corresponding author:
Md Yeasin Bhuiyan, Department of Mechanical Engineering, University of South Carolina, 300 Main Street, Room#A237, Columbia, SC 29208-0001, USA.
Email: yeasin85@gmail.com

Recently, Chang et al.[5] described the damage index (DI) comparison for NDE and SHM techniques and showed the variation of DI with the crack size. Using piezo-enabled spectral element analysis, one transmitter PWAS is used to generate ultrasonic waves in the plate and three receiver PWAS transducers are used to sense the scattered signal coming from the rivet hole with butterfly cracks. The motivation and importance of analyzing the rivet hole cracks have emanated from these researches. The multiple-rivet-hole lap joint crack problem stipulates the interaction of Lamb waves from multiple directions.

Lamb wave scattering from various types of damages has been analyzed by many researchers.[6,7] Moreau et al.[8] analyzed the scattering of fundamental Lamb and SH wave from flat-bottomed cavities in a plate. However, their vector projection method considered a finite number of scattered modes to determine the unknown coefficients and a rule of thumb was used select the number of modes required for proper convergence. The longitudinal and shear wave scattering in two-dimensional geometry and a spherical geometry had been analyzed using finite element method (FEM) modeling.[9] However, the plate guided wave (Lamb and SH wave) modeling with rivet hole crack type damage was yet to be considered. In these researches, the simulated signal was not produced to detect the damage. Chang et al.[10] used the hybrid global local method to investigate the rivet hole of a plate with infinite dimension and then extended his model for the rivet hole with cracks. However, the single Lamb wave mode incidence was studied using FEM in the local damage model. The simulation using the analytical formulation with finite difference method (FDM) for a fatigue crack and a notch in a hole was performed by Fromme et al.[11] The piezoelectric transducer was used to excite first antisymmetric mode for the experiment. Recent researches have put emphasis on the simulated results using fast and efficient numerical techniques to understand the Lamb wave behavior prior to the implementation of the results in the physical structures.[12] Numerical methods are becoming the popular tool for understanding the complex Lamb wave interaction problems with complicated boundary conditions.[13,14] The scattered field of a single rivet hole cracks with single directed (incident) Lamb wave has been described introducing the wave damage interaction coefficient (WDIC) and the nonreflective boundary (NRB) was implemented to the simulate the infinite plate in a successful manner.[15] However, unidirectional Lamb wave interaction with the rivet hole damage was considered to verify the effectiveness of the NRB modeling in FEM.

Scope of the article

The novelty of this article is that we considered multidirectional Lamb wave scattering from a butterfly cracked rivet hole using local FEM. Then, we implemented the FEM results in our analytical framework to obtain the real-time simulated signal that could potentially indicate the sensitive location of sensor installation. Both symmetric and antisymmetric Lamb wave modes are impinging on the rivet hole with cracks from multiple directions. Local 3D finite element model has been created for each incident Lamb wave to perform the harmonic analysis. WDICs are calculated along the all possible azimuthal positions of the damage. This has been performed for all incident directions of Lamb waves. The "scatter cube" (Figure 1(b)) of WDICs are formed for the scattered wave modes that can be imported to the analytical framework of wave propagation analysis. An example of the design of sensor installation has been demonstrated as the Lamb wave incident at 18° to the butterfly cracked rivet hole.

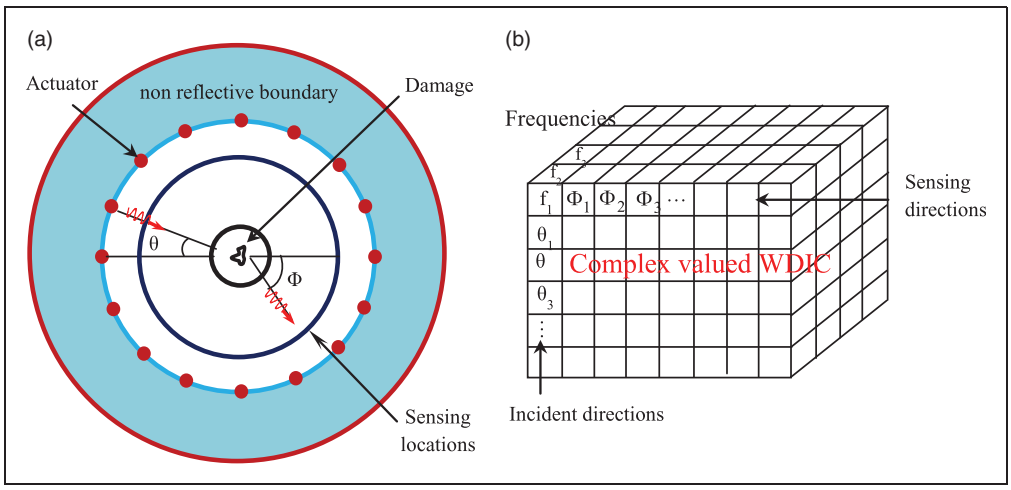

Figure 1. (a) Representative FE model; (b) "scatter cube" of WDICs.

Interaction of Lamb wave with damage

Incident Lamb wave

Lamb waves generated from the transmitter transducers hitting the damage from multiple directions are shown in Figure 1(a). Lamb waves undergo scattering and mode conversion upon interaction with the damage. The scattered field is captured by another set of receiver transducers around the damage for each direction of the incident Lamb wave. Lamb wave outward propagation from a point source can be described using the thickness-dependent mode shape $a_n(z)$ and the Hankel function of order one ($H_1^{(1)}(\xi_n r)$) by the following equation[16]

$$u_r = \sum_{n=1}^{\infty} a_n(z) H_1^{(1)}(\xi_n r) e^{-i\omega t} \tag{1}$$

where n represents the Lamb wave mode shape number. The wavenumber ξ follows the Rayleigh–Lamb equation[17]

$$\frac{\tan \eta_s d}{\tan \eta_p d} = \left[\frac{-4\eta_p \eta_s \xi^2}{\left(\xi^2 - \eta_s^2\right)^2} \right]^{\pm 1} \tag{2}$$

where $2d$ is the plate thickness.

$$\eta_p^2 = \frac{\omega^2}{c_p^2} - \xi^2; \quad \eta_s^2 = \frac{\omega^2}{c_s^2} - \xi^2; \quad c_p = \sqrt{\frac{\lambda + 2\mu}{\rho}}; \quad c_s = \sqrt{\frac{\mu}{\rho}} \tag{3}$$

where the exponent $+1$ and -1 refer to the symmetric and antisymmetric Lamb wave modes, respectively. c_p is the pressure wave speed and c_s is the shear wave speed; λ, μ, ρ are the Lame's constants and density of the host material. The detailed solution of the Lamb wave can be found in Giurgiutiu[16] and Graff[17] and will not be discussed for the sake of brevity.

Scattered SH wave

Due to the interaction of Lamb waves with the damage mode, conversion happens and a portion of the Lamb waves are converted to the shear horizontal (SH) waves. The SH waves irradiating from an axisymmetric point source can be derived starting from the governing equation, i.e.

$$\nabla^2 u_\theta = \frac{\partial^2 u_\theta}{\partial r^2} + \frac{1}{r}\frac{\partial u_\theta}{\partial r} - \frac{u_\theta}{r^2} + \frac{\partial^2 u_\theta}{\partial z^2} = \frac{1}{c_s^2}\frac{\partial^2 u_\theta}{\partial t^2} \tag{4}$$

Assuming a harmonic wave field and using the method of separation of variables, i.e.

$$u_\theta = b_n(z) U_\theta(r) e^{-i\omega t}; \quad \frac{\partial^2 u_\theta}{\partial t^2} = -\omega^2 u_\theta \tag{5}$$

where u_θ is the radial displacement, $b_n(z)$ is the mode shape of the nth SH mode, and ω is the circular frequency. Substitution of equation (5) into equation (4) yields (see appendix for detail derivation)

$$\left(\xi^{SH} r\right)^2 \frac{\partial^2 U_\theta}{\partial (\xi^{SH} r)^2} + \left(\xi^{SH} r\right) \frac{\partial U_\theta}{\partial (\xi^{SH} r)} + \left\{ \left(\xi^{SH} r\right)^2 - 1 \right\} U_\theta = 0 \tag{6}$$

where ξ^{SH} is the SH wavenumber. The solution of equation (6) follows the first kind Hankel function of order one, $H_1^{(1)}\left(\xi_n^{SH} r\right)$ for outward propagating waves and substituting into equation (5) yields

$$u_\theta = \sum_{n=1}^{\infty} b_n(z) H_1^{(1)}\left(\xi_n^{SH} r\right) e^{-i\omega t} \tag{7}$$

The wavenumber follows the characteristic equation given by

$$\eta_s = \frac{n\pi}{2d} \tag{8}$$

where $n = 0, 2, 4, \ldots,$ (symmetric modes) and $n = 1, 3, 5, \ldots,$ (antisymmetric modes).

Complex-valued WDIC for scattered Lamb wave and SH wave

Along the sensing circle, there exist two types of waves namely, direct incident waves and scattered waves. Thus, the total wavefield at any sensing node would be the superposition of the incident and scattered wave fields, i.e.

$$\psi_{TOTAL} = \psi_{IN} + \psi_{SC} \tag{9}$$

Following equation (9), the incident wave fields need to be subtracted from the total wave field in order to get the field scattered wave. In FE analysis, the sensing node wave field of the pristine model (Figure 2) gives the field of the incident wave, while the damaged model provides the total wavefields. Hence, subtracting the pristine wave fields from the damaged wave fields gives the scattered wavefield along the sensing boundary around the damage.

The displacements of scattered waves at the top and bottom nodes of the sensing circle (Figure 3) are required to separate the Lamb wave and SH wave modes. The radial components of the displacement (u_r^T and u_r^B) at the top and bottom surface provide Lamb wave modes (at top node), as follows

$$u_{SC}^{S0} = \frac{u_r^T + u_r^B}{2}; \quad u_{SC}^{A0} = \frac{u_r^T - u_r^B}{2} \tag{10}$$

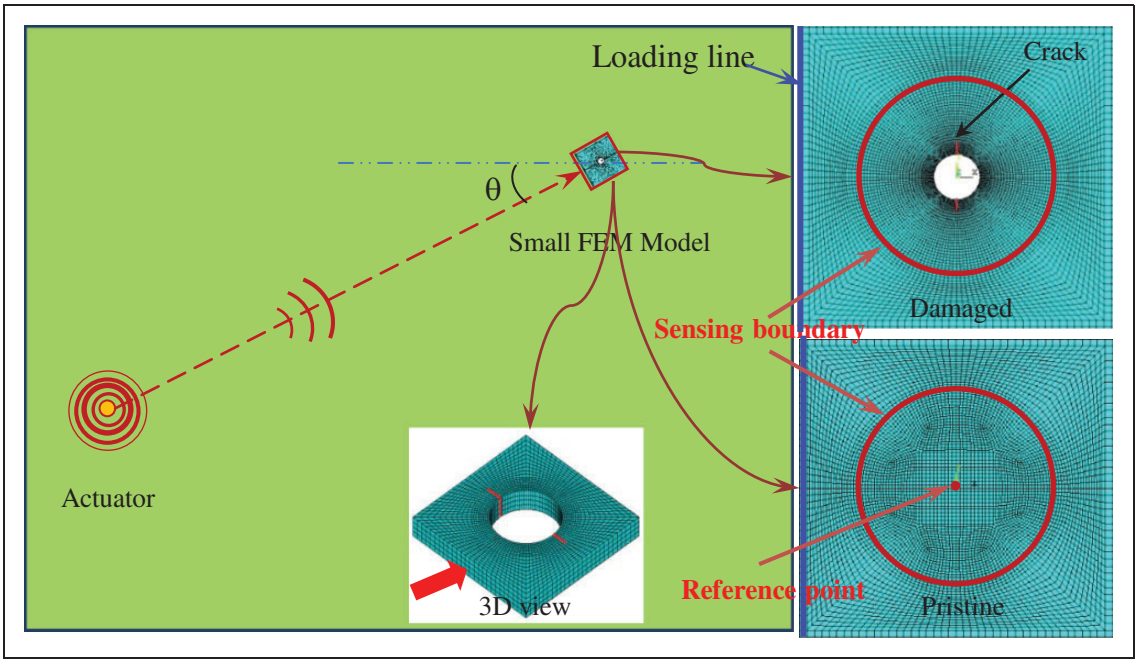

Figure 2. Smaller local FEM model for the Lamb wave incident from an arbitrary direction.

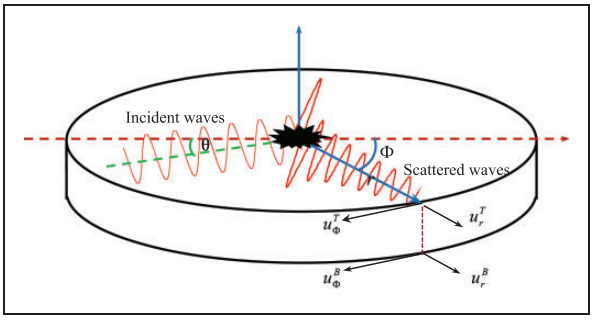

Figure 3. Extraction of WDIC from a small-size finite element model.

The tangential components of the displacement (u_Φ^T and u_Φ^B) at the top–bottom nodes of the sensing circle provide the SH wave modes (at top node), i.e.

$$u_{SC}^{SH_{S0}} = \frac{u_\Phi^T + u_\Phi^B}{2}; \qquad u_{SC}^{SH_{A0}} = \frac{u_\Phi^T - u_\Phi^B}{2} \tag{11}$$

The displacement field of the incident wave (u_{IN}) may be recorded from the reference point of Figure 2 through the FE analysis of the pristine model. The incident displacement field coming toward the center of the damage and the scattered displacement field recorded at the sensing circle follow a certain relation[18] i.e.

$$\begin{aligned} &U_{IN}^A e^{-i\varphi_{IN}^A} C_{AB}(\omega,\theta,\Phi) e^{-i\varphi_{\mathrm{AB}}(\omega,\theta,\Phi)} H_m^{(1)}\left(\xi^B r\right) \\ &\quad = U_{SC}^B(\omega,\theta,\Phi) e^{-i\varphi_{SC}^B(\omega,\theta,\Phi)} \end{aligned} \tag{12}$$

where $U_{IN}^{\mathrm{A}} e^{-i\varphi_{IN}^{\mathrm{A}}}$ represents any incident mode A at the center of the damage; $C_{AB}(\omega,\theta,\Phi)e^{-i\varphi_{AB}(\omega,\theta,\Phi)}$ represents the amplitude $C_{AB}(\omega,\theta,\Phi)$ and phase $e^{-i\varphi_{AB}(\omega,\theta,\Phi)}$ of WDIC; $H_m^{(1)}(\xi^B r)$ is the Hankel function of 2D scattered wave field (B) propagates in an outward direction with $m = 1$. C_{AB} stands for the incident A wave mode to the scattered B wave mode that depends on the direction of incident Lamb wave, azimuthal direction of the damage and the circular frequency. On the right side $U_{SC}^B(\omega,\theta,\Phi)e^{-i\varphi_{SC}^B(\omega,\theta,\Phi)}$ represents the scattered displacement field along the sensing boundary of radius r.

Upon rearrangement, equation (12) yields

$$\begin{aligned} &C_{AB}(\omega,\theta,\Phi)e^{-i\varphi_{AB}(\omega,\theta,\Phi)} \\ &\quad = \frac{U_{SC}^B(\omega,\theta,\Phi)}{U_{IN}^A} \frac{1}{H_m^{(1)}(\xi^B r)} e^{-i\Delta\varphi_{AB}(\omega,\theta,\Phi)} \end{aligned} \tag{13}$$

where, $\Delta\varphi_{\mathrm{AB}}(\omega,\theta,\Phi) = \varphi_{SC}^B(\omega,\theta,\Phi) - \varphi_{IN}^A$. From equation (13), the amplitude and phase may be separated as

$$C_{AB}(\omega,\theta,\Phi) = \left| \frac{U_{sc}^B(\omega,\theta,\Phi)}{U_{IN}^A} \frac{1}{H_m^{(1)}(\xi^B r)} \right| \tag{14}$$

$$\begin{aligned} \varphi_{AB}(\omega,\theta,\Phi) &= \Delta\varphi_{AB}(\omega,\theta,\Phi) \\ &\quad - \left[\angle \frac{1}{H_m^{(1)}(\xi^B r)} - \angle \frac{1}{H_m^{(1)}(0^+)} \right] \end{aligned} \tag{15}$$

For instance, when incident symmetric Lamb wave mode (S0 mode) causes scattered S0 mode then both A and B corresponds to the parameters of S0 mode. When incident S0 mode causes scattered symmetric

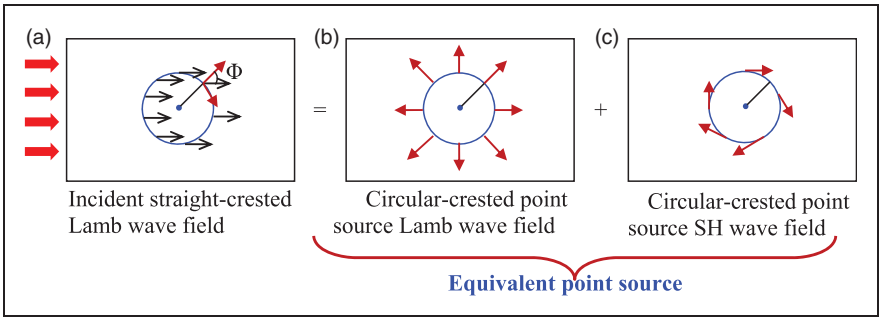

Figure 4. Equivalent source of a straight-crested Lamb wave (the drawn arrows in (b), (c) are representative purposes only, not in actual scale). (a) Incident straight-crested Lamb wave field; (b) circular-crested point source Lamb wave field; (c) circular-crested point source SH wave field.

SH mode then A corresponds to the parameters of S0 mode but B corresponds to the SH wave mode.

Analytical WDIC for a simple case

We choose a simple pristine plate (Figure 4) to demonstrate the analytical WDIC. For the pristine plate, it may be possible to derive the analytical expression of the WDIC.

Let us consider a plane wavefront Lamb waves travel in the $+x$ direction in an infinite plate. It generates a uniform wave field all over the pristine plate. At any sensing circle of radius r, the wave fields are shown in Figure 4(a) that can be replaced by an equivalent source in Figure 4(b) and (c). The equivalent source (ES) can be considered as the superposition of the two circular crested point Lamb and SH wave point sources that take care of the radial and tangential components of the incident wave field, respectively. Thus we may write

$$\psi_{StarightLW} = \psi_{CircularLW} + \psi_{CircularSH} \tag{16}$$

Analytical derivation of WDIC

The incident displacement field $\vec{u}_i$ for the straight-crested Lamb wave can be written as

$$\vec{u}_i = \begin{bmatrix} u_x^{IN} \\ 0 \\ u_z^{IN} \end{bmatrix} (\text{Cartesiancoordinates}) \tag{17}$$

$$\vec{u}_i = \begin{bmatrix} u_x^{IN}\cos(\Phi) \\ -u_x^{IN}\sin(\Phi) \\ u_z^{IN} \end{bmatrix} (\text{cylindricalcoordinates}) \tag{18}$$

The displacement field $\vec{u}_{ES}$ of the equivalent source placed at the origin O equalizes the incident displacement field $\vec{u}_i$, i.e.

$$\vec{u}_i = \vec{u}_{ES} \tag{19}$$

The equivalent displacement is the vector sum of Lamb and SH wave displacements as

$$\vec{u}_{ES} = \vec{u}_{ES}^{LW} + \vec{u}_{ES}^{SH} \tag{20}$$

The Lamb wave displacement field has components in the radial and thickness direction only whereas the SH wave displacement field has component in the tangential direction only, i.e.

$$\vec{u}_{ES}^{LW} = \begin{bmatrix} u_r^{ES} H_1^{(1)}(\xi_{LW} r) \\ 0 \\ u_z^{IN} \end{bmatrix}; \quad \vec{u}_{ES}^{SH} = \begin{bmatrix} 0 \\ u_\Phi^{ES} H_1^{(1)}(\xi_{SH} r) \\ 0 \end{bmatrix} \tag{21}$$

where, u_r^{ES} and u_Φ^{ES} represent the amplitude of the circular crested Lamb and SH wave displacement fields; $H_1^{(1)}$ is the first kind first-order Hankel function.

Substituting equation (21) into equation (20), and then into equation (19) yields

$$\begin{aligned} u_r^{ES} H_1^{(1)}(\xi_{LW}.r) &= u_x^{IN}\cos(\Phi); \\ u_\Phi^{ES} H_1^{(1)}(\xi_{SH}.r) &= -u_x^{IN}\sin(\Phi) \end{aligned} \tag{22}$$

Normalizing equation (22) by the incident displacement (u_x^{IN}) and taking magnitude, WDICs of the Lamb and SH waves can be obtained as

$$WDIC_{LW} = |C_{LW}\cos\Phi|; \qquad WDIC_{SH} = |C_{SH}\sin\Phi| \tag{23}$$

where, $C_{LW} = 1 \Big/ H_1^{(1)}(\xi_{LW}.r)$ and $C_{SH} = 1 \Big/ H_1^{(1)}(\xi_{SH}.r)$ depend on frequency-dependent wave number ξ and sensing circle radius r. The expressions of the WDICs are much simpler for the pristine plate. They depend on the azimuthal direction Φ only for a certain frequency and sensing circle.

Plot of analytical WDIC and comparison with FEM

The polar plots of the analytical WDICs (WDIC profiles) take the ideal double circle shape as shown in Figure 5(a) and (b). In this case, the Lamb wave

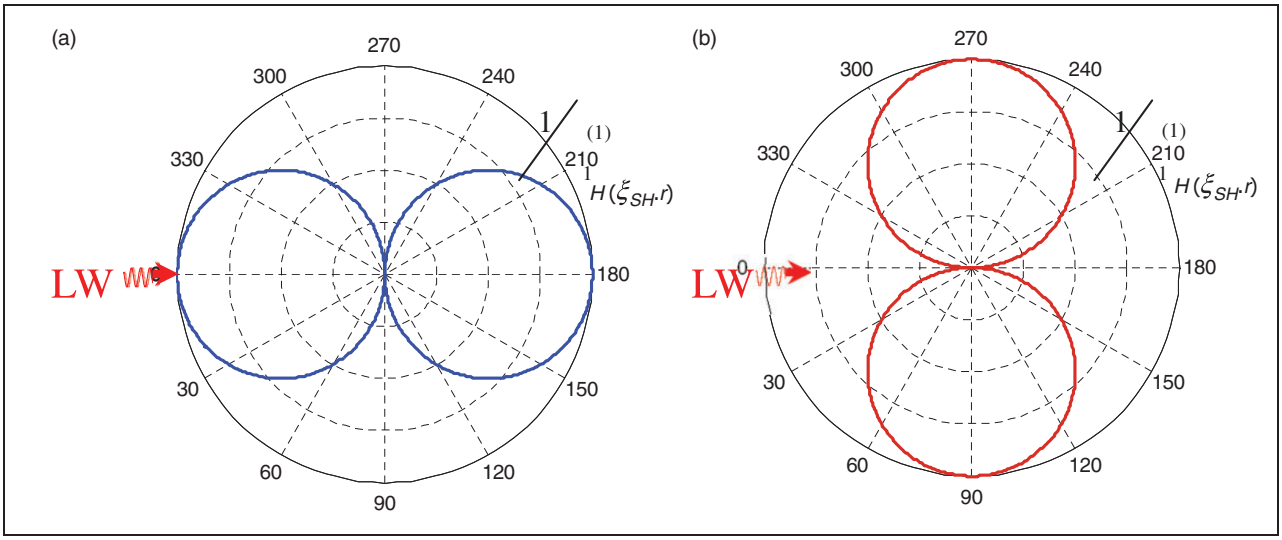

Figure 5. Analytical (a) $WDIC_{LW\_LW}$; (b) $WDIC_{LW\_SH}$.

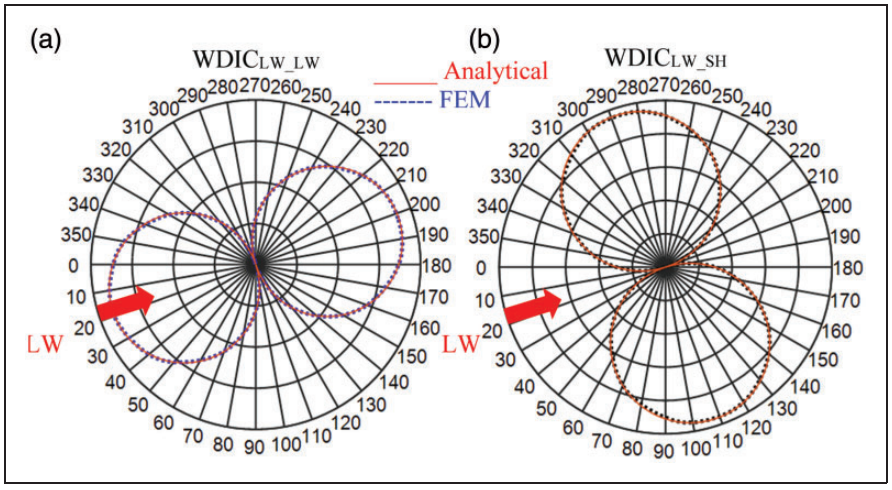

Figure 6. Analytical and FEM comparison of (a) $WDIC_{LW\_LW}$; (b) $WDIC_{LW\_SH}$.

incident horizontally to the pristine plate as shown by the red sign (Figure 5(a) and (b)). It can be noticed that the Lamb waves are guided forward and backward direction whereas the SH waves are guided transversely. As the Lamb wave incident at $\theta = 18^{\circ}$ to the horizontal line (Figure 6), the double-circle $WDIC_{S0\_S0}$ and $WDIC_{S0\_SH0}$ also tilted by the same amount of inclination. The ideal shapes maintain symmetry about the incident line and its perpendicular line.

The WDIC profiles obtained analytically and from the FEM are shown in Figure 5 for both Lamb wave and SH wave; it shows that both of them follow a very good agreement. Since the plate boundary conditions are symmetric, scattered antisymmetric wave mode do not appear for symmetric incident Lamb wave mode.

Description of the finite element modeling

The exact analytical formulations are used to generate the Lamb waves from the transmitter PWAS including the propagation up to the local damage.[16] The damage interaction are obtained by extracting WDICs from the FE analysis. The harmonic analyses are performed on a local small size (40 mm × 40 mm) 3D FE model for each incident Lamb wave. The NRBs of 20 mm wide on each side is used effectively to minimize the interference of the boundary reflections.[15,19]

Imposition of load

The analytical formulations of straight-crested Lamb modes are used to calculate the nodal forces since the damage is assumed far away from the transmitter. It is a valid assumption because the circular-crested Lamb waves emanating from the transmitter behave like the straight-crested Lamb waves at large distances from the source.[16] The 3D view of the local FEM model is shown in Figure 7(a). Incoming Lamb waves are shown as three red signal signs on one face of the model. Lamb mode excitation is imposed through

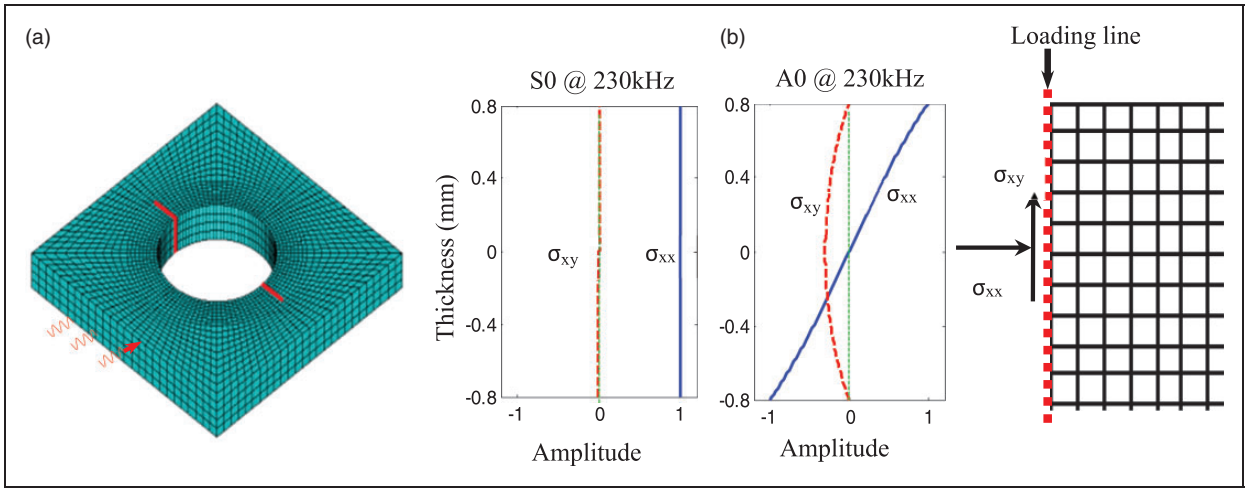

Figure 7. (a) Small FEM model; (b) exaggerated view of mode shapes and FE loading lines in the thickness direction.

nodal forces by evaluating integrals of stress mode shape components on the loading nodes. The stress mode shapes are calculated analytically[16] and converted into nodal forces through boundary integration on each element along the loading line. The element nodal force can be evaluated by using the following equation[20]

$$F_{ix}^{e} = \int_0^{L_e} \sigma_{xx}^{e}(s) N_i^{e}(s) \mathrm{d}s; \quad F_{iy}^{e} = \int_0^{L_e} \sigma_{xy}^{e}(s) N_i^{e}(s) \mathrm{d}s \tag{24}$$

where subscript and superscript e stands for the element, L_e represents the element size, F_{ix}^{e} and F_{iy}^{e} are nodal forces in x and y directions, i is the element node number, and $N_i^{e}(s)$ is the shape function of selected element type.

The stress mode shapes and loading line along a single line on that face are shown in Figure 7(b). The stress mode shapes are given by:

Symmetric modes

$$\begin{aligned}
\sigma_{xx}^{S}(x,y,t) &= C^{S} 2\mu\xi\eta_S \left[\left(\xi^2 + \eta_S^2 - 2\eta_P^2\right)\cos\eta_S \mathrm{d}\cos\eta_P y - \left(\xi^2 - \eta_S^2\right)\cos\eta_P \mathrm{d}\cos\eta_S y\right] e^{i(\xi x - \omega t)} \\
\sigma_{yy}^{S}(x,y,t) &= -C^{S} 2\mu\xi\eta_S \left(\xi^2 - \eta_S^2\right)\left(\cos\eta_S \mathrm{d}\cos\eta_P y - \cos\eta_P \mathrm{d}\cos\eta_S y\right) e^{i(\xi x - \omega t)} \\
\sigma_{xy}^{S}(x,y,t) &= iC^{S}\mu\left[4\xi^2\eta_P\eta_S\cos\eta_S \mathrm{d}\sin\eta_P y + \left(\xi^2 - \eta_S^2\right)^2\cos\eta_P \mathrm{d}\sin\eta_S y\right] e^{i(\xi x - \omega t)}
\end{aligned} \tag{25}$$

Antisymmetric modes

$$\begin{aligned}
\sigma_{xx}^{A}(x,y,t) &= -C^{A} 2\mu\xi\eta_S \left[\left(\xi^2 + \eta_S^2 - 2\eta_P^2\right)\sin\eta_S d\sin\eta_P y - \left(\xi^2 - \eta_S^2\right)\sin\eta_P d\sin\eta_S y\right] e^{i(\xi x - \omega t)} \\
\sigma_{yy}^{A}(x,y,t) &= C^{A} 2\mu\xi\eta_S \left(\xi^2 - \eta_S^2\right)\left(\sin\eta_S d\sin\eta_P y - \sin\eta_P d\sin\eta_S y\right) e^{i(\xi x - \omega t)} \\
\sigma_{xy}^{A}(x,y,t) &= iC^{A}\mu\left[4\xi^2\eta_P\eta_S\sin\eta_S d\cos\eta_P y + \left(\xi^2 - \eta_S^2\right)^2\sin\eta_P d\cos\eta_S y\right] e^{i(\xi x - \omega t)}
\end{aligned} \tag{26}$$

The nodal forces are updated for each calculation step, imposing Lamb mode excitation for each excitation frequency.

Modeling of the crack

Cracks in the rivet hole are modeled using the discontinuity at the adjacent pair of nodes along the cracks. There are actually two sets of nodes along the crack faces and each set is representing the nodes on each face and the nodes are discontinuous along the crack faces. Two sets of nodes are adjacent to each other unlike the modeling of the notch where there is a small gap between those sets of nodes. Like the nodes, the solid elements are also disbanded along the crack faces. The modeling of the cracks in finite element using the above approach is fair enough to model the actual cracks of rivet hole in the plate-like structure.[21] In this modeling, a crack length of 1.6 mm on each side of the rivet hole is considered. This small size of the crack indicates the crack initiation during the fatigue crack growth. In this analysis, the crack

length-to-hole diameter ratio was 0.5. The rivet hole dimension was chosen based on the commonly used aircraft fastening hole of 6.4 mm (1/4 inches).

Impinging Lamb waves from multiple directions

The problem of butterfly rivet hole cracks is symmetric in terms of the direction of the incident about the line of cracks and the line perpendicular to it. Hence, the results obtained for 0 to $+90^\circ$ incident Lamb wave can be used to produce the results for 0 to -90°. And the results of the other side of the line of cracks would be the mirror image of the 0 to $+90^\circ$ and 0 to -90° results. Thus, the FE analyses are performed for 0 to $+90^\circ$angles of the incident Lamb wave with an interval of 9°. New FE model is created for each direction of Lamb wave incident. The displacement fields at the top and bottom surface of the plate along the sensing boundary is captured for each direction of Lamb wave incident. The results for any other angle of incident Lamb wave may be obtained by the interpolation between the results of two consecutive incident directions.

Meshing, imposing NRB, and validation of the FE model

The calculation burden is far reduced by implementing NRBs around the local small size model. NRBs allow to simulate the wave propagation in infinite medium without any interference of the edge reflections. Eight-node SOLID45 structural elements are used for meshing the local model of the plate, whereas the spring-damper elements (COMBIN14) are used to model the NRBs. An aircraft grade aluminum-2024-T3 plate of 1.6 mmthickness is used. A mesh size of 0.4 mmis adopted along the thickness, which is fair enough to capture the thickness mode shapes. To capture the high gradient of stresses, finer meshes are used near the crack region. Relatively coarser meshes are adopted in the region away from the crack as well as the exterior region of the sensing circle. The proper meshing and NRBs are implemented in the studies of Shen and Giurgiutiu.[15,18] The FE results are validated with the results obtained for Lamb wave incident at 0° in Shen and Giurgiutiu.[18] Moreover, the analytical WDIC profiles maintain very good conformity with the FEM WDIC profiles for the pristine plate as shown in Figure 6.

The frequency domain of the harmonic analysis is selected based on the dispersion curves of Lamb waves[17] to keep the wave modes within the fundamental Lamb wave and SH wave modes. The step of the frequency is kept at 2 kHz with an upper range of 900 kHz. At very close to the crack region, there are evanescent wave modes or local vibrations that die out within a short distance from the damage source. The radius of the sensing circle is chosen such that only propagating wave modes are being captured along the sensing locations. Three FE simulations are executed for each direction of the Lamb wave incident to obtain the effect of cracks in each case: interaction of Lamb waves with (1) butterfly cracked rivet hole in the plate, (2) only rivet hole in the plate, (3) pristine plate. Subtraction methods are used to find out the effect of cracks following equation (9). The pristine plate wave fields provide the required direct incident wave fields in equation (14).

The scatter cubes are generated from complex-valued WDICs of the cracks as indicated by Figure 1(b). The three dimensions of the scatter cube contain the WDICs for the variation of frequencies, angles of transmitting PWASs, and angles of sensing PWASs. The scatter cube is obtained for each scattered wave mode. The scatter cubes provide the information of the complicated 3D interaction of Lamb waves with the local damage from multiple directions.

Discussion of the results

WDIC profile for the cracks

In Figure 8, the evolution of the WDIC profiles are shown. It indicates that, in presence of hole type damage in the plate, the WDIC profile gets distorted from its ideal double circle shape. Meaning, at a certain direction the scattered wave amplitude is higher than the other directions and the sensor could be placed in that direction to capture the presence of hole damage. In case of hole with cracks, the WDIC profile gets additionally distorted and no more symmetry can be observed. It shows some location around that damage where it is scattering wave at relatively higher amplitude than an arbitrary direction. The higher WDIC indicates the higher amplitude of the wave and stronger receiving signal by the sensors. For the illustration purpose, the S0 Lamb wave mode is considered to be incident at $\theta = 18^\circ$ with a frequency of 500 kHz.

In Figure 8, the WDIC of the hole (only) can be obtained by subtracting the pristine profile (a) from the damaged (hole) profile (b) and the WDIC of crack (only) can be obtained by the subtraction of hole (b) from the hole+crack (c). The individual effect of the damage can clearly be observed from Figure 9(a) and (b).

Frequency domain and azimuthal variation of WDIC of the cracks

As the frequency changes, the magnitude of WDIC changes for each direction of the Lamb wave incident. There exist some frequencies for which WDIC reaches higher values. The variation WDIC_{S0_S0} over the range of frequency is shown in Figure 10. For example, when Lamb wave hits the damage at $\theta = 18^\circ$, WDIC reaches maximum at 618 kHz (S0 mode). We

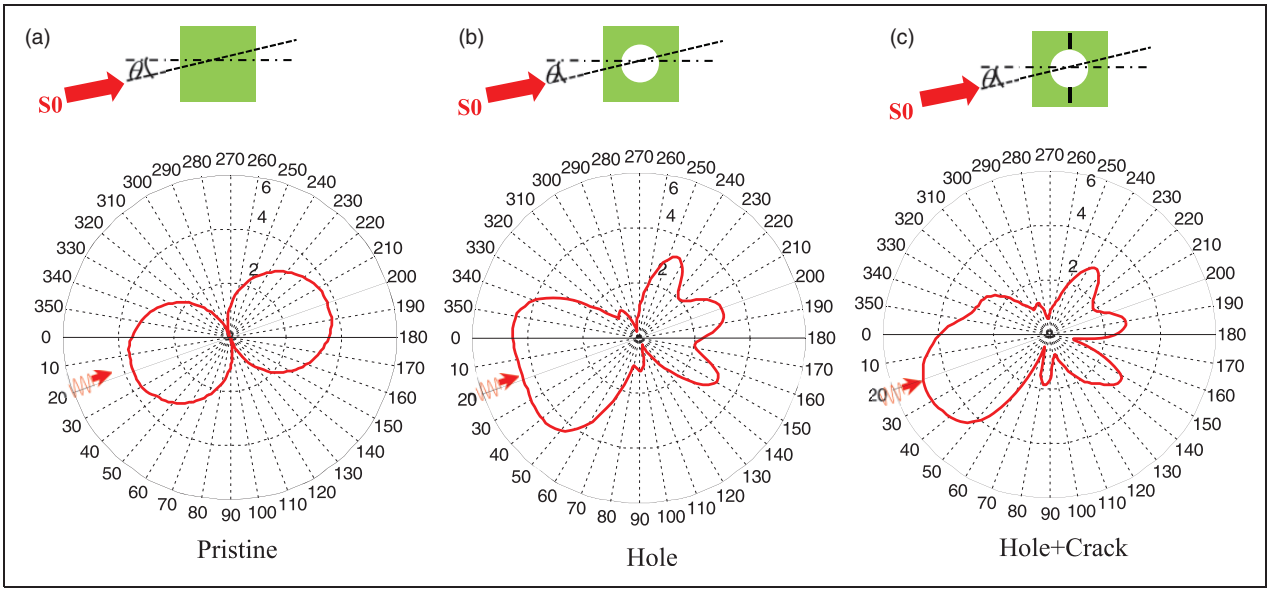

Figure 8. The variation of the WDIC profiles under different damage situations (S0 Lamb mode incident at $\theta = 18^{\circ}$, $f = 500$ kHz): (a) pristine; (b) hole; (c) hole + crack.

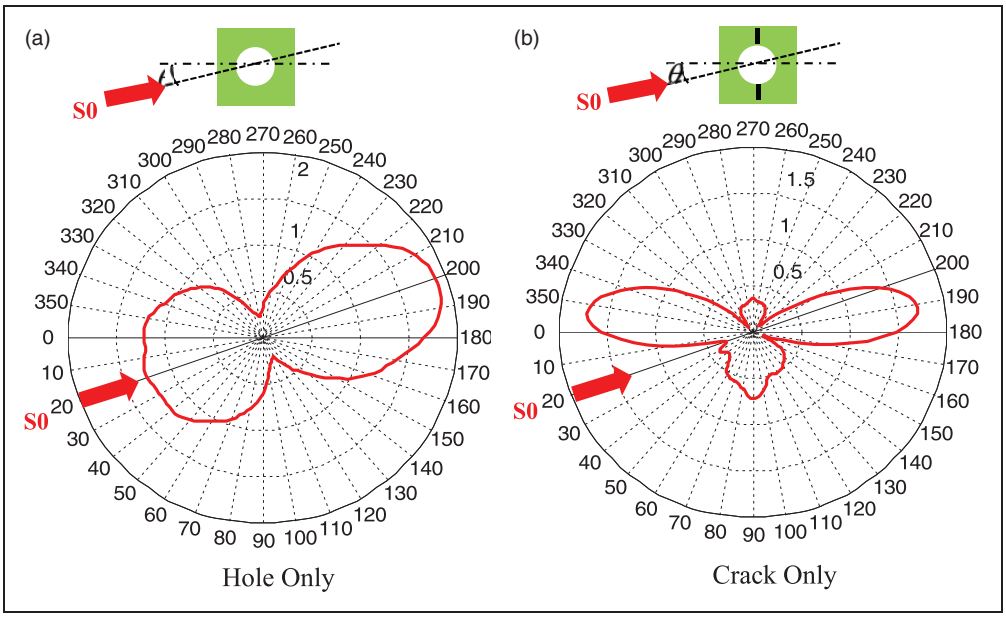

Figure 9. WDIC profiles for hole only and crack only (S0 Lamb mode incident at $\theta = 18^{\circ}$, $f = 500$ kHz).

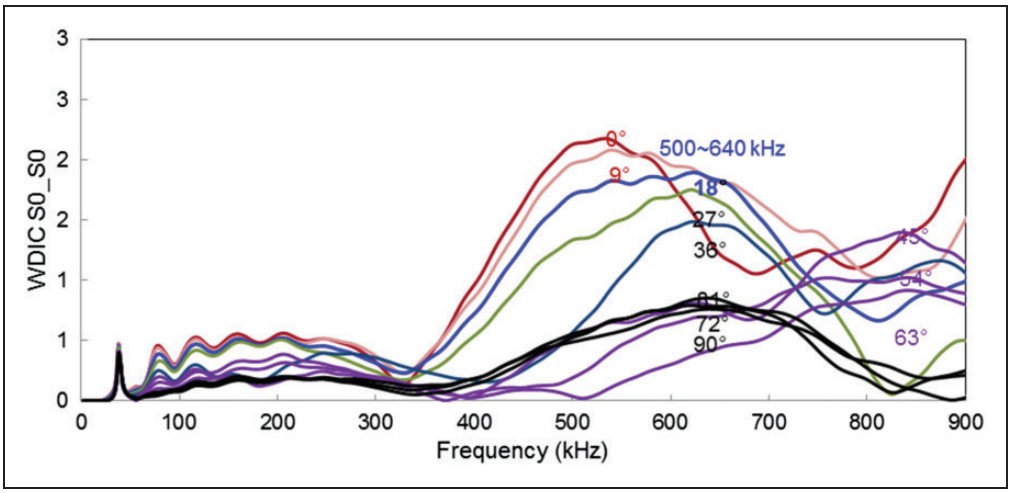

Figure 10. Frequency domain variation of $WDIC_{S0\_S0}$ incident Lamb waves from multiple directions (at most sensitive location).

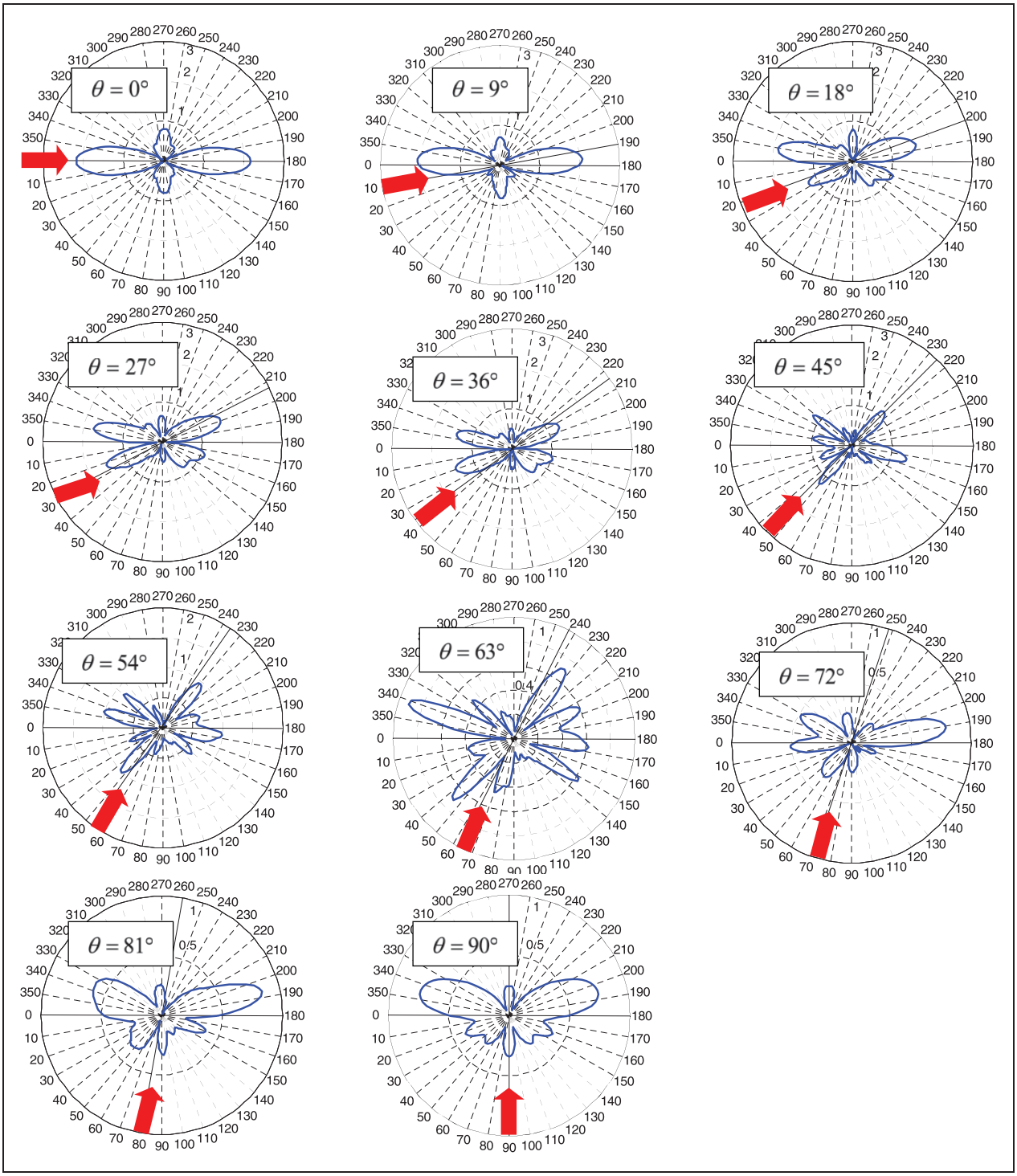

Figure 11. Azimuthal variation of $WDIC_{S0\_S0}$ for multiple incident directions (at most sensitive frequencies).

call them "most sensitive frequency". The higher value of WDIC gives the better signal in the receiver.

The WDIC also varies with the azimuthal position of the sensor. For most sensitive excitation frequency, not all azimuthal positions are equally sensitive. For example, at $\theta = 18°$, the maximum WDIC occurs at azimuthal position $\Phi = 350°$("most sensitive location").

The variation of $WDIC_{S0\_S0}$ with the azimuthal position is shown in Figure 11 for each direction of the Lamb wave incident. As the angle of incidence increases, the WDIC of scattered Lamb wave decreases.

The most sensitive frequency for incident A0 Lamb wave mode ($\theta = 18°$) is around 300 kHz(Figure 12) and similar analysis can be

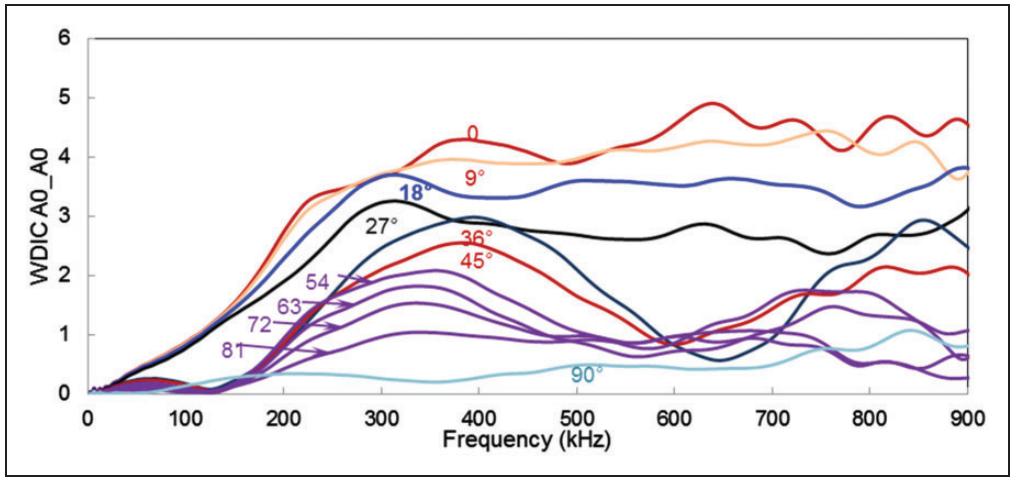

Figure 12. Frequency domain variation of $WDIC_{A0\_A0}$ incident Lamb waves from multiple directions (at most sensitive location).

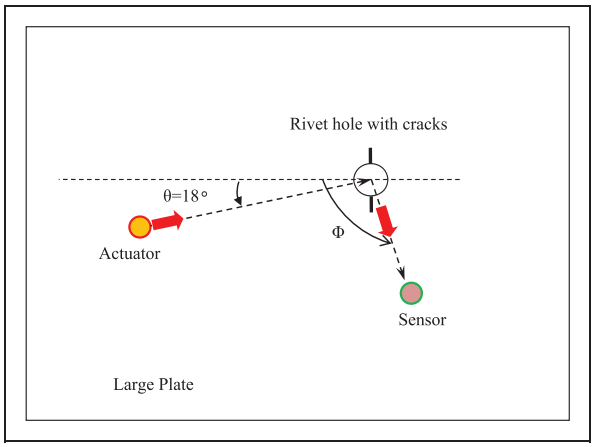

Figure 13. Illustration of the actuator and sensor installation around the cracked rivet hole in a large plate.

performed to obtain the sensitive location. The azimuthal variation of $WDIC_{A0\_A0}$ for different angles of the incident has not been shown here for the sake of brevity.

Application: Time domain signals using analytical model

Now we discuss the application of the scatter cube to analyze a specific case of a cracked rivet hole as shown Figure 13. We want to know the frequency of excitation signal from the actuator and the optimum location of the sensor around that damage. From the geometry of the rivet hole and actuator position, it is possible to calculate the direction of the incident Lamb wave to the damage.

To illustrate an example, we consider the Lamb wave incident at $\theta = 18^\circ$ to one of the rivet hole with cracks. The propagation of the Lamb wave from the transmitter up to the local damage and the propagation of scattered wave from the local damage up to the receiver sensor can be determined using the exact analytical formulation. The scattering and mode conversion information are fed through the scatter cube of WDIC obtained using the FE analysis. The details of the analytical framework that utilizes the damage information can be found in Shen and Giurgiutiu[18] and is not repeated here.

Figure 14 illustrates the importance of selecting the optimum parameters (both frequency and location) of sensor installment. It also demonstrates how the WDIC affect the time domain signal that is actually received by the sensor. For illustration purpose, four different cases (these are selected based on the frequency and azimuth domain analysis mentioned in Figure 10 and 11) are considered corresponding to different magnitudes of WDIC such as

(a) $f = 320$ kHz, $\Phi = 350^\circ$(this frequency and location corresponds to low WDIC)
(b) $f = 486$ kHz, $\Phi = 350^\circ$(moderately high WDIC)
(c) $f = 618$ kHz, $\Phi = 350^\circ$(high WDIC)
(d) $f = 618$ kHz, $\Phi = 75^\circ$(the frequency is most sensitive but for the bad location of receiver sensor)

The signal produced in Figure 14 represents the signal due to the presence of the crack in the hole only, meaning, the signal of the hole is subtracted from the signal of the hole+crack. By observing the time domain signal of Figure 14, the obvious selection of parameter is either (b) or (c), because they give the most sensible signal. Thus, the excitation frequency of 486–618 kHz at the transmitter and the receiver sensor at $\Phi = 350^\circ$ is the optimum design parameter for detecting the cracks in that rivet hole. We may do similar analysis for any rivet hole present in the plate and determine the optimum positions of the receiver and then we can optimize the required number of sensors.

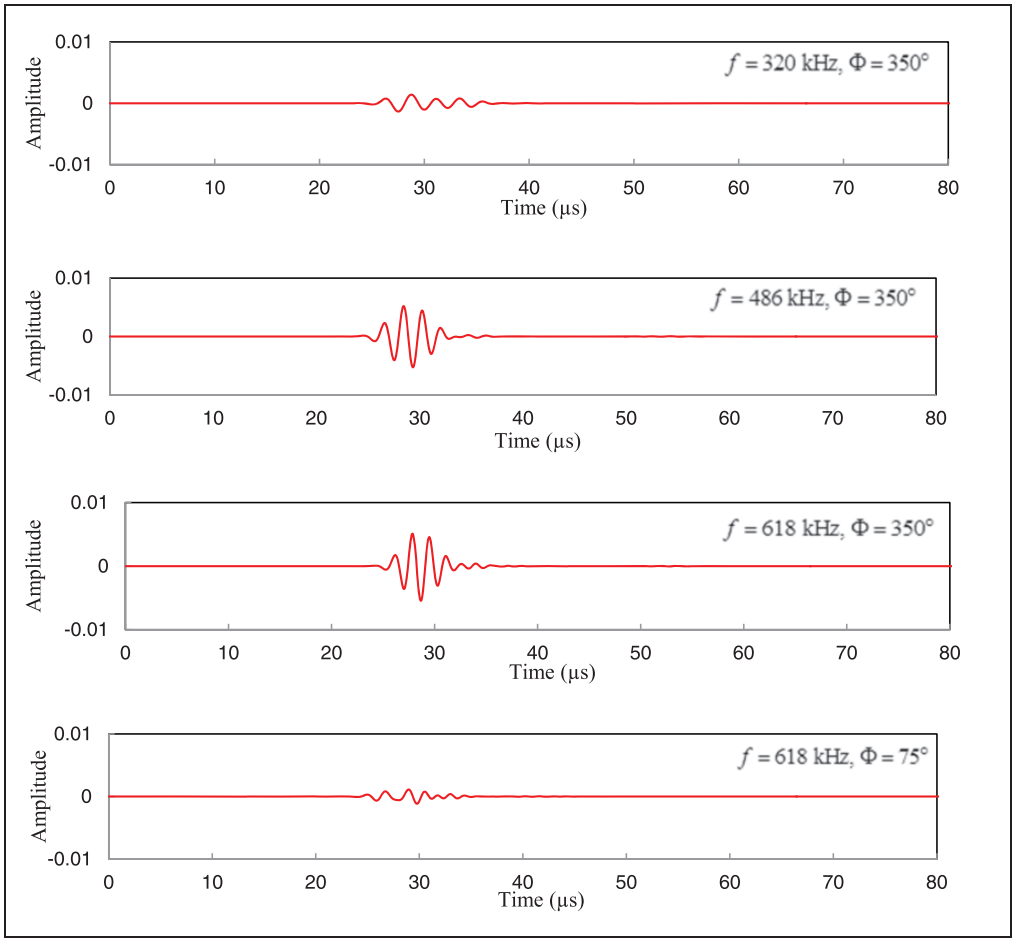

Figure 14. Sensing signals patterns for different selection of parameters (frequency and location) ($\theta = 18°$).

Conclusion

Interaction of the Lamb waves with rivet hole cracks from multiple directions has been described by the complex-valued wave damage interaction coefficients. FE analyses have been used to determine the WDICs that involve scattering and mode conversion. SH waves appear in the scattered waves besides the Lamb waves because of the mode conversion. Local small-sized damage model with proper NRB is analyzed for efficient FE analysis. WDIC profile for the pristine case is developed analytically and comparison with the FE results shows very good agreement. The scattered fields in the presence of cracks are obtained through the subtraction process and corresponding WDIC shows the frequency of excitation and azimuthal location dependency. The higher magnitude of WDIC gives the better signal in the receiver. Scatter cubes of WDICs are obtained that contain the scatter field information over the frequency domain around the damage, and all possible directions of incident Lamb wave modes (S0, A0). At the end, a problem of multiple-rivet-hole cracks is addressed and the optimum frequency of transmitter and location of the receiver are obtained for a particular incident of Lamb waves. Using the scatter cube and exact analytical framework, the time domain signals are produced to confirm the detection of cracks in the rivet hole.

Future work

An experiment may be designed based on the simulated results to detect the cracks in the rivet holes with the Lamb wave incident from multiple directions. The design may be developed for detecting the cracks in the multiple-rivet-hole lap joint by considering the interaction among the rivet holes. The FEM simulation can be extended for different hole sizes and crack lengths. Analyzing the WDIC profile and corresponding time domain signal, it is possible to estimate the smallest detectable hole and crack size. The hole–hole interaction can be included for multiple adjacent rivet holes present in the structures.

Acknowledgement

The authors would like to thank the Technical Representative, Dr Ignacio Perez.

Declaration of Conflicting Interests

The author(s) declared no potential conflicts of interest with respect to the research, authorship, and/or publication of this article.

Funding

The author(s) disclosed receipt of the following financial support for the research, authorship, and/or publication of this article: This research work was supported by the Office of Naval Research (grant number N000141410655).

References

1. Thompson RB, Brasche LH, Forsyth D, et al. Recent advances in model-assisted probability of detection. In: *4th European-American workshop on reliability of NDE*, Berlin, Germany, 23–26 June 2009.
2. Harding CA, Hugo GR and Bowles SJ. Model-assisted POD for ultrasonic detection of cracks at fastener holes. *Rev Quant Nondestruct Eval* 2006; 820: 1862–1869.
3. Bode MD, Newcomer J and Fitchett S. Transfer function model-assisted probability of detection for lap joint multi site damage detection. In: *The 31th review of progress in quantitative nondestructive evaluation*, Burlington, VT, 2012, vol. 1430, pp.1749–1756.
4. Schubert Kabban CM, Greenwell BM, DeSimio MP, et al. The probability of detection for structural health monitoring systems: Repeated measures data. *Struct Health Monitor* 2015; 14: 252–264.
5. Chang F-K, Janapati V, Kopsaftopoulos F, et al. Quantification of structural health monitoring for damage detection. In: *The 30th Aircraft Structural Integrity Program (ASIP)*, 2014.
6. Lu Y, Ye L, Su Z, et al. Quantitative assessment of through-thickness crack size based on Lamb wave scattering in aluminium plates. *NDT E Int* 2008; 41: 59–68.
7. Golato A, Demirli R and Santhanam S. Lamb wave scattering by a symmetric pair of surface-breaking cracks in a plate. *Wave Motion* 2014; 51: 1349–1363.
8. Moreau L, Caleap M, Velichko A, et al. Scattering of guided waves by flat-bottomed cavities with irregular shapes. *Wave Motion* 2012; 49: 375–387.
9. Velichko A and Wilcox PD. Efficient finite element modeling of elastodynamic scattering with non-reflecting boundary conditions. *Rev Prog Quant Nondestruct Eval* 2012; 31: 142–149.
10. Chang Z and Mal A. Scattering of Lamb waves from a rivet hole with edge cracks. *Mech Mater* 1999; 31: 197–204.
11. Fromme P and Sayir MB. Detection of cracks at rivet holes using guided waves. *Ultrasonics* 2002; 40: 199–203.
12. Grahn T. Lamb wave scattering from a circular partly through-thickness hole in a plate. *Wave Motion* 2003; 37: 63–80.
13. Glushkov E, Glushkova N, Eremin A, et al. Low-cost simulation of guided wave propagation in notched plate-like structures. *J Sound Vib* 2015; 352: 80–91.
14. Wang S, Huang S and Zhao W. Simulation of Lamb wave's interactions with transverse internal defects in an elastic plate. *Ultrasonics* 2011; 51: 432–440.
15. Shen Y and Giurgiutiu V. Effective non-reflective boundary for Lamb waves: Theory, finite element implementation, and applications. *Wave Motion* 2015; 58: 22–41.
16. Giurgiutiu V. *Structural health monitoring with piezoelectric wafer active sensors*. 2nd ed. London: Elsevier Academic Press, 2014.
17. Graff KF. *Wave motion in elastic solids*. Dover: Oxford University Press, 1991.
18. Shen Y and Giurgiutiu V. Combined analytical FEM approach for efficient simulation of Lamb wave damage detection. *Ultrasonics* 2016; 69: 116–128.
19. Bhuiyan MY, Shen Y and Giurgiutiu V. Guided wave based crack detection in the rivet hole using global analytical with local FEM approach. *Materials* 2016; 9: 602.
20. Reddy JN. *An introduction to the finite element method*. 3rd ed. New York: McGraw-Hill, 2006.
21. Trendafoilova I, Gorman DG and Manoach E. An investigation on vibration-based damage detection in circular plates. *Struct Health Monitor* 2009; 8: 291–302.

Appendix

Governing equation for SH wave

$$\nabla^2 u_\theta = \frac{\partial^2 u_\theta}{\partial r^2} + \frac{1}{r}\frac{\partial u_\theta}{\partial r} - \frac{u_\theta}{r^2} + \frac{\partial^2 u_\theta}{\partial z^2} = \frac{1}{c_s^2}\frac{\partial^2 u_\theta}{\partial t^2} \tag{27}$$

Assuming a harmonic wave field and using the method of separation of variables, i.e.

$$u_\theta = b_n(z)U_\theta(r)e^{-i\omega t}; \quad \frac{\partial^2 u_\theta}{\partial t^2} = -\omega^2 u_\theta \tag{28}$$

where u_θ is the radial displacement, $b_n(z)$ is the mode shape of the nth SH mode, ω is the circular frequency.

Substitution of equation (28) into equation (27) yields

$$\left[\frac{\mathrm{d}^2 U_\theta}{\mathrm{d}r^2} + \frac{1}{r}\frac{\mathrm{d}U_\theta}{\mathrm{d}r} - \frac{1}{r^2}U_\theta\right] b_n e^{-i\omega t} + \frac{\mathrm{d}^2 b_n}{\mathrm{d}z^2}U_\theta e^{-i\omega t} = -\frac{\omega^2}{c_s^2}U_\theta b_n e^{-i\omega t} \tag{29}$$

Dividing by $U_\theta b_n e^{-i\omega t}$ and rearranging, equation (29) yields

$$\left[\frac{\mathrm{d}^2 U_\theta}{\mathrm{d}r^2} + \frac{1}{r}\frac{\mathrm{d}U_\theta}{\mathrm{d}r} - \frac{1}{r^2}U_\theta + \frac{\omega^2}{c_s^2}U_\theta\right]\frac{1}{U_\theta} = -\frac{1}{b_n}\frac{\mathrm{d}^2 b_n}{\mathrm{d}z^2} = \eta_s^2 \tag{30}$$

where η_s^2 is the separation constant.

Multiplying by U_θ, one of the equations of (30) become

$$\frac{\mathrm{d}^2 U_\theta}{\mathrm{d}r^2} + \frac{1}{r}\frac{\mathrm{d}U_\theta}{\mathrm{d}r} - \frac{1}{r^2}U_\theta + \frac{\omega^2}{c_s^2}U_\theta = \eta_s^2 U_\theta \tag{31}$$

Rearranging

$$\frac{\mathrm{d}^2 U_\theta}{\mathrm{d}r^2} + \frac{1}{r}\frac{\mathrm{d}U_\theta}{\mathrm{d}r} + \left(\frac{\omega^2}{c_s^2} - \eta_s^2 - \frac{1}{r^2}\right) U_\theta = 0 \tag{32}$$

Multiplying by r^2 and inserting $\xi^{SH^2} = \omega^2/c_s^2 - \eta_s^2$, equation (32) yields

$$r^2 \frac{d^2 U_\theta}{dr^2} + r\frac{\mathrm{d}U_\theta}{dr} + (\xi^{SH^2} r^2 - 1) U_\theta = 0 \tag{33}$$

Multiplying and dividing first two terms by ξ^{SH^2}, equation (33) yields

$$\left(\xi^{SH} r\right)^2 \frac{\partial^2 U_\theta}{\partial(\xi^{SH} r)^2} + \left(\xi^{SH} r\right)\frac{\partial U_\theta}{\partial(\xi^{SH} r)} + \left\{\left(\xi^{SH} r\right)^2 - 1\right\} U_\theta = 0 \tag{34}$$

Radial displacements (u_r) propagation of Lamb wave is given as

$$u_r = \sum_{n=1}^{\infty} a_n^{LW}(z) H_1^{(1)}\left(\xi_n^{LW} r\right) e^{-i\omega t} \tag{35}$$